

# Lattice thermal conductivity of half-Heuslers with density functional theory and machine learning: Enhancing predictivity by active sampling with principal component analysis

Rasmus Tranås<sup>a</sup>, Ole Martin Løvvik<sup>b,c</sup>, Oliver Tomic<sup>d</sup>, Kristian Berland<sup>a</sup>

<sup>a</sup>*Department of Mechanical Engineering and Technology Management, Norwegian University of Life Sciences, Drøbakveien 31, Ås, 1432, Ås, Norway*

<sup>b</sup>*Centre for Materials Science and Nanotechnology, Department of Physics, University of Oslo, Sem Sælands vei 26, Oslo, 0371, Oslo, Norway*

<sup>c</sup>*Materials Physics, SINTEF, Forskningsveien 1, Oslo, 0373, Oslo, Norway*

<sup>d</sup>*Department of Data Science, Norwegian University of Life Sciences, Drøbakveien 31, Ås, 1432, Ås, Norway*

---

## Abstract

Low lattice thermal conductivity is essential for high thermoelectric performance of a material. Lattice thermal conductivity is often computed based on density functional theory calculations, but such calculations carry a high computational cost and machine learning is therefore increasingly being used to estimate lattice thermal conductivity at a much lower computational expense. With the ability to assess larger sets of materials, machine learning could offer an effective procedure to identify low lattice thermal conductivity compounds. However, such compounds can be quite rare and distinct from typical compounds in a given training set. This can be problematic as standard machine learning methods lack the ability to precisely interpret properties of compounds with features differing significantly from those in the training set. By computing the lattice thermal conductivity of 122 half-Heusler compounds using the temperature dependent effective potential method, we generate a data set sufficient in span to explore this issue. We show that random forest regression can fail to identify low lattice thermal conductivity compounds with random selection of training data. However, if the choice of training data is instead guided using feature and principal component analysis, it can drastically improve the ability to identify low lattice thermal conductivity compounds as well as model performance.

---

## 1. Introduction

With their ability to convert heat to electricity, thermoelectrics find use in a number of niche technologies ranging from wine coolers, hiking stoves with mobile phone chargers, and radioisotope thermoelectric (TE) generators used to power e.g. the *Curiosity* Mars rover. Thermoelectrics also have a great potential to reduce global greenhouse gas emission through waste heat recovery, but their role is currently limited by the modest efficacy realized in devices [1, 2] and the fact that several state-of-the-art TE materials contain toxic or rare elements [3, 4]. Finding new TE materials has therefore gathered much scientific interest in recent years [5].

The efficiency of TE materials is conventionally given by the dimensionless figure of merit, which is expressed as  $ZT = \sigma S^2 T / (\kappa_e + \kappa_\ell)$ , where  $\sigma$  is the electrical conductivity,  $S$  is the Seebeck coefficient,  $T$  is the absolute temperature,  $\kappa_e$  is the electronic thermal conductivity, and  $\kappa_\ell$  is the lattice thermal conductivity. A high  $ZT$  requires both a high power factor,  $\mathcal{P} = \sigma S^2$ , and simultaneously a low total thermal conductivity. In non-metals,  $\kappa_\ell$  is typically significantly larger than  $\kappa_e$ , while in heavily doped semiconductors,  $\kappa_\ell$  and  $\kappa_e$  can be comparable in size [6, 7]; nonetheless, a low  $\kappa_\ell$  is usually important for achieving high  $ZT$ .

High-throughput screening studies based on first-principle calculations have in recent years been used to discover new TE materials [8–14]. Some studies focus on electronic properties and use simple models or estimates of  $\kappa_\ell$ . This could be because calculations of  $\kappa_\ell$  can become computationally expensive. The computational cost arises because accounting for the phonon-phonon interactions due to the anharmonicity of the lattice vibrations requires obtaining third-order force constants extracted from a large number of supercell-based density functional theory (DFT) calculations [15–17]. For this reason, machine learning (ML) methods are increasingly supplementing first-principles based calculations for predicting  $\kappa_\ell$  [18–25], and pre-trained ML models have been used in a convenient web-based application [26].

The half-Heusler (HH) compounds are a class of cubic compounds with three atoms in the primitive

cell, belonging to the  $F\bar{4}3m$  spacegroup. As shown in Fig. 1, the  $XZ$  sublattice forms a rocksalt structure, while the  $YZ$  sublattice forms a zinc-blende structure [27–29]. Several HH compounds have a high power factor in combination with relatively low  $\kappa_\ell$ , making HHs attractive for TE applications [8, 13, 30–36]. Recently, Feng et al. [37] used DFT-based calculations to show that the four HH compounds: CdPNa, BaBiK, LaRhTe, and LaPtSb have very low  $\kappa_\ell$ . LaPtSb and BaBiK have also have promising electronic transport properties in addition to low  $\kappa_\ell$  and could have a  $ZT$  competitive with the top performing TE materials [38–40]. Because  $\kappa_\ell$  of these four compounds is much lower than that of typical HH compounds, the set of HH compounds presents itself as a dataset well suited for investigating ML methods to separate low and high  $\kappa_\ell$  compounds. The high symmetry of HHs also reduces the computational cost of calculating  $\kappa_\ell$  compared to more complex material systems such as layered compounds and compounds with distorted symmetries [41–43]. The reduced cost allows us to generate both training and validation sets for assessing  $\kappa_\ell$ .

Our study is based on 122 HH compounds for which  $\kappa_\ell$  is computed explicitly using DFT. The compounds are based on a combination of dynamically stable HHs, 54 from groups 4-9-15 (Ti,Zr,Hf)(Co,Rh,Ir)(As,Sb,Bi), 4-10-14 (Ti,Zr,Hf)(Ni,Pd,Pt)(Ge,Sn,Pb), and 48 HHs from groups 5-8-15 (V,Nb,Ta)(Fe,Ru,Os)(As,Sb,Bi) and 5-9-14 (V,Nb,Ta)(Co,Rh,Ir)(Ge,Sn,Pb). The last 20

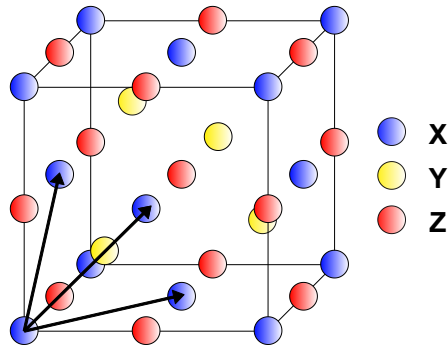


Fig. 1: The HH crystal structure, displayed as the unit cell. The primitive cell is made from the three atoms X, Y, and Z.

HHs are the remaining stable compounds studied by Feng et al. [37], based on a revision of the 75 stable HHs identified by Carrete et al. [18].

## 2. METHODS

### 2.1. Lattice thermal conductivity

DFT calculations in this work are done with the VASP [44–46] software package using the revision of Perdew-Burke-Ernzerhof generalized gradient approximation for solids (PBEsol) [47, 48]. The plane-wave energy cutoff is set to 600 eV. For the relaxations, we use an  $11 \times 11 \times 11$   $\mathbf{k}$ -point sampling of the Brillouin zone, while the electronic self-consistent loop is iterated to an energy difference of  $10^{-6}$  eV, and ionic positions are relaxed until forces fall below 1 meV/Å. The lattice thermal conductivity,  $\kappa_\ell$ , is calculated with the temperature dependent effective potential (TDEP) method [16, 49], taking into account three-phonon and isotope-phonon scattering [50, 51]. Fifty configurations based on  $3 \times 3 \times 3$  repetitions of the primitive cell are used to obtain second- and third-order force constants. The atomic configurations are taken from a fixed-temperature canonical ensemble at 300 K, where the zero-point motion of the phonons is matched with the Debye temperature [52]. The Debye temperature is obtained from the Voigt approximation of the bulk and shear moduli [53]. A  $3 \times 3 \times 3$   $\mathbf{k}$ -point grid is used for the supercell DFT force calculations. We employ a cutoff for second-order pair-interactions of 7 Å while for third-order pair-interactions, the cutoff is set slightly larger than half the width of the supercell (i.e. 6.1 Å for NbCoGe). For the calculation of  $\kappa_\ell$ , the reciprocal space is discretized on a  $35 \times 35 \times 35$   $\mathbf{q}$ -point grid. In a detailed convergence study for NbCoGe, we find this choice of parameters to give a numerical error of  $\kappa_\ell$  less than 3 %.

### 2.2. Machine learning model

Random forest (RF) regression is a non-linear ML method used in industry and academia alike [54]. An RF model is based on an ensemble of decision trees, where each tree is trained on a subset of randomly

chosen features and training samples. This randomness makes RF less prone to overfitting. RF has been shown to perform well in earlier ML studies involving the lattice thermal conductivity [23]. In the RF regression, a given input sample is sorted in each of the decision trees based on its features, so that in a given tree, the sample is assigned to a  $\kappa_\ell^{\{i..j\}}$  in the training set. Finally, the predicted outcome is given by the mean  $\langle \kappa_\ell^{\{i..j\}} \rangle$  of the predictions of the ensemble of decision trees.

In ML, failing to identify key features can result in overfitting and reduce method interpretability [55, 56]. Feature selection is here performed using exhaustive feature selection (EFS) in combination with RF regression. EFS is a brute-force scheme to assess the predictive performance of every possible combination of extracted features. This is computationally costly when a large number of features is involved, but in our study this cost is small compared to that of computing  $\kappa_\ell$ . The EFS model finds the subset of features that gives the best outcome of a chosen performance metric using cross-validation with the training data. The optimal features for a training set is here chosen as the subset of features that gives the highest Spearman rank correlation between predicted and calculated  $\kappa_\ell$  in a five-fold cross-validation process. The EFS scheme is done with the MLXTEND [57] code, while RF regression is done using SCIKIT-LEARN [58]. Note that in each case when a set of features is evaluated, the hyperparameters of the RF model are optimized independently with a hyperparameter grid search.

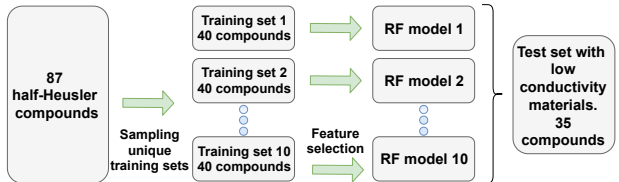


Fig. 2: Flowchart for building the baseline model.

Fig. 2 outlines the construction of the baseline model. In the model, 87 out of the 122 compounds are semi-randomly selected as the training pool for ML, while 35 are left out as a test set used for model as-

essment. By semi-randomly, we refer to that the five lowest  $\kappa_\ell$  compounds are in the test set. We make this choice to emulate a not too improbable scenario that could easily arise for larger material classes when only modest size training sets are used. From the training pool, 10 unique training sets of 40 compounds are selected randomly. EFS using RF regression is then done for each of the training sets. The models are then retrained based on the features obtained with EFS. Our baseline model predictions is given by the average of the predictions of these 10 RF models.

In the alternative active sampling model, we use principal component analysis (PCA) with the HOGGORM [59] package to identify compounds possessing combinations of feature values that make them distinct from those in the training pool. PCA takes into account correlations between features and provides orthogonal principal components (PC) as linear combinations of feature vectors in feature space. The PCs are oriented in the direction of maximum variance in feature space. In the procedure the features are centered and scaled to unit variance. The PCA analysis is based on all compounds in the study. Using PCA, we identify three compounds that are needed to cover the feature space mapped out by the first four PCs. These three are subsequently included in the training sets from the baseline model, such that the 10 training sets for the active sampling model contain 43 compounds which are used with RF and EFS.

Our study is based on 14 features, out of which the following nine are tabulated features: the ratio between the lightest and heaviest atoms in the primitive cell [60],  $m_r$ , the average atomic mass,  $m_a$ , the standard deviation of the atomic masses,  $m_s = 1/3 \left( \sum_{i=X,Y,Z} (m_i - m_a)^2 \right)^{1/2}$ , as well as corresponding features for the electronegativity [61],  $\chi$ , and covalent atomic radius [62],  $r$ . An additional five features is based on standard output of low-cost DFT calculations. These include the following: the volume of relaxed primitive unit cell,  $V$ , and mass density,  $\rho$ . We also include the lattice thermal conductivity of the Slack model [63],  $\kappa_s$ , Debye temperature,  $\theta_D$ , and bulk modulus,  $B$ , which are related to the elastic tensor [64]. In other works, several higher-order features have been shown to be

linked to scattering of phonons, such as the three-phonon scattering phase space, effective spring constants, and first moment frequencies from the phonon density of states [18, 37, 65]. Using such features can improve the predictions of the ML model, but we here limit the features to those that are based on properties one can expect to be continuously added in large material databases such as the MATERIALSPROJECT [66]. Therefore, using such simple features supports a methodology which can later be adopted for screening of larger material databases, and the features can be assessed for other material classes.

### 3. RESULTS AND DISCUSSION

#### 3.1. Lattice thermal conductivity of half-Heusler compounds

Fig. 3 compares the lattice thermal conductivity calculated with the TDEP method,  $\kappa_\ell^{\text{TDEP}}$ , at 300 K, 500 K, and 700 K for the 122 HHs. Table A.1, Appendix A, reports  $\kappa_\ell^{\text{TDEP}}$  at 500 K. The span of  $\kappa_\ell^{\text{TDEP}}$  goes from 0.85 W/mK (LaPtSb) to 23.45 W/mK (LiBSi) at 500 K, revealing that the chemical composition affects thermal transport notably. Compounds with heavy atoms on the  $X$ - or  $Z$ -site, such as La, Ba, Bi, and Pb, or with high average mass, typically have lower  $\kappa_\ell^{\text{TDEP}}$ . The correlation between lattice thermal conductivity and the average mass has been observed for experimental lattice thermal conductivity with compounds across different spacegroups [20]. The ordering of the five lowest  $\kappa_\ell^{\text{TDEP}}$  materials from low to high  $\kappa_\ell^{\text{TDEP}}$  is consistent with what was found by Feng et al. [37]. The vanadium-containing compounds VRuBi, VFeBi, VIrPb, VOsBi, VRhPb, and VCoPb are found to have negative phonon frequencies and are not studied further. The two latter have previously been found to have favorable decomposition into elemental phases [67].

In the following, the ML models are based on  $\kappa_\ell^{\text{TDEP}}$  at 500 K, which also would be indicative of low lattice thermal conductivity at 300 and 700 K.



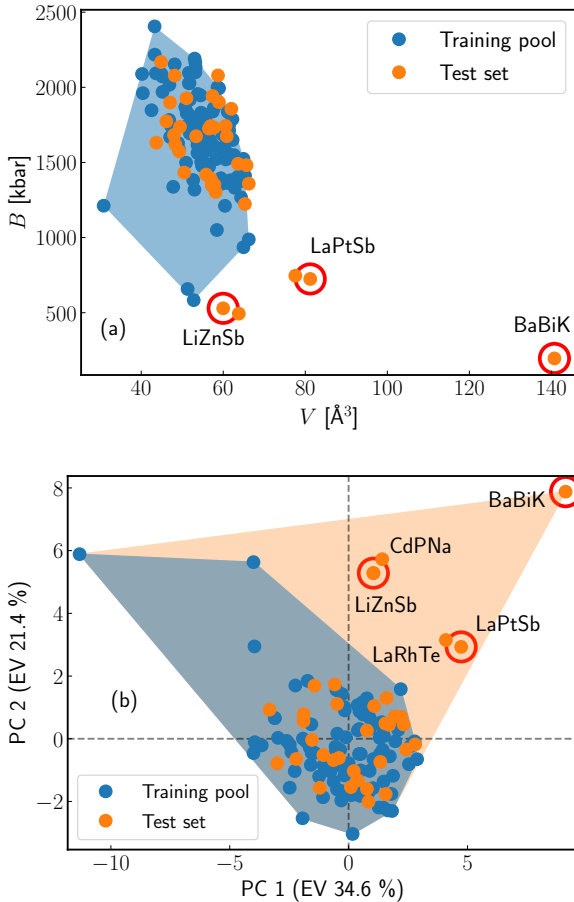


Fig. 4: (a) Scatter plot of the two most important features from the EFS,  $V$  (x-axis) and  $B$  (y-axis). (b) PCA for the HH compounds using all 14 features. The first PC is shown on the x-axis and the second is on the y-axis. The blue region is the area of the PC space spanned by the 87 materials in the training pool, while the orange region is the space spanned with inclusion of the test compounds.

### 3.2. Using principal component analysis for diversifying training sets

Fig. 4 (a) shows the position of the compounds in the space spanned by  $V$  and  $B$ , two features known to be related to lattice thermal conductivity [18, 20, 68]. In general, low  $V$  materials will tend to have less compressed acoustical phonon band structures, increasing the phonon group velocity [69] and thus also the

lattice thermal conductivity. Higher  $B$  can also be related to stiffer atomic bonds and increased phonon velocities. This is in line with the Spearman correlation of  $-0.69$  between  $\kappa_{\ell}^{\text{TDEP}}$  and  $V$  and  $0.58$  between  $\kappa_{\ell}^{\text{TDEP}}$  and  $B$  for the compounds in the training pool. The plot shows that some of the compounds in the test set fall outside the convex hull spanned by  $V$  and  $B$  of the compounds in the training pool. By including such outliers in the training sets, we can possibly diversify the ML models. However, as  $B$  and  $V$  also have a sizeable Spearman correlation of  $-0.51$ , —i.e. higher  $V$  tend to be related to less stiff bonds and thus lower  $B$  — solely relying on these two features carries a risk of missing important compounds and correlations. This motivates the use of PCA, which offers a more systematic procedure to take all features and their correlations into consideration.

Fig. 4 (b) indicates the position of the compounds of the test set and training pool in the subspace spanned by the two first PCs. This subspace accounts for 56.0 % of the cumulative explained variance (EV) of the feature space<sup>1</sup>, while the first four PCs account for 79.1 % cumulative EV. Two convex hull are shown in the figure: the blue spans the training pool and the orange spans the remaining domain of the test compounds. In the two dimensional PC space, the low  $\kappa_{\ell}$  compounds clearly lie outside of the linear span of the features in the training pool.

To facilitate ML interpolation, we identify three additional compounds that are included in the training sets of the active sampling model. These compounds are highlighted with red circles in Fig. 4. The specific compounds to be included are determined iteratively by identifying the compounds in the test set with the largest euclidean distance in the PC space to those in the current training pool, until a marked drop in distance arises. This procedure identifies that the three additional compounds BaBiK, LiZnSb, and LaPtSb should be included in the training set.

<sup>1</sup>When the two PCs are mapped back to the original feature space, the cumulative explained variances of  $V$  and  $B$  are 78.6 % and 77.2 %, showing that the PCs retain most of the information for these features.

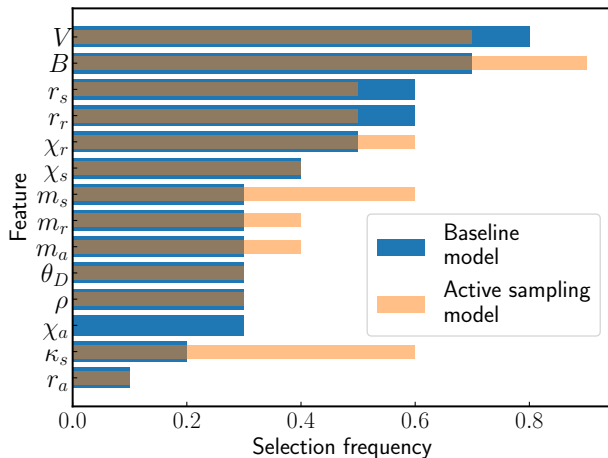


Fig. 5: Selection frequencies for the 14 features in the EFS using RF regression for the baseline (blue bars) and active sampling (orange bars) models.

### 3.3. Exhaustive feature selection analysis

Fig. 5 compares the selection frequency of a given feature in the EFS for the 10 RF models used in the baseline (blue bars) and active sampling (orange bars) ML models. The baseline and active sampling models use on average 5.7 and 6.3 features out of the 14 potential features, respectively. The relatively few features used is in line with the recent results of Miyazaki et al. [70] showing that using a limited feature subset gives the best ML performance, as overfitting can arise with redundant features. In both the baseline and active sampling models,  $B$  and  $V$  are the most frequently selected features, which agrees with their high Spearman correlation with  $\kappa_\ell^{\text{TDEP}}$  as discussed in the previous section. However, while both these features are simultaneously selected despite a relatively high inter-correlation, this is not the case for all features. For instance, in the active sampling model, only one of the 10 models select both  $V$  and  $\kappa_s$  at the same time, with a correlation of -0.79, whereas six include both  $B$  and  $\kappa_s$ , which have a correlation of 0.34.

There are some notable differences between the EFS for the active sampling model compared to the baseline model. In particular, the selection frequency of  $m_s$  increases from 0.3 to 0.6 for the active sam-

Table 1: Performance metrics for predicting  $\log(\kappa_\ell^{\text{TDEP}})$  for the 32 test compounds using the active sampling and baseline models. The metrics are R2-score, RMSE, Spearman correlation, and Pearson correlation. The standard deviations are in parenthesis.

	Active	Baseline
R2	0.86 (0.03)	0.32 (0.16)
RMSE	0.21 (0.02)	0.46 (0.05)
SC	0.83 (0.07)	0.77 (0.09)
PC	0.94 (0.02)	0.61 (0.13)

pling model. This result reflects that the variation of masses in the primitive cell is linked to low lattice thermal conductivity, such as the case of BaBiK. The selection frequency for  $\kappa_s$  and  $B$  also sees an increase for this model.

### 3.4. Enhanced machine learning performance with active sampling

Fig. 6 (a) compares the predictions made by the baseline model and the active sampling model using the logarithmic scale used in the training. The error bars indicate the standard deviation in the prediction of the 10 models. It shows that the active sampling method has a superior ability to identify the compounds with low  $\kappa_\ell^{\text{TDEP}}$ . The three compounds found with PCA, highlighted with red circles, are not predicted by the active sampling model, as they are included in the training process. Fig. 6 (b) shows the corresponding comparison with a linear scale. In this case, the compounds are sorted according to  $\kappa_\ell^{\text{TDEP}}$ . In most of the cases, the predictions of the active sampling method,  $\kappa_\ell^{\text{AS}}$ , is higher than  $\kappa_\ell^{\text{TDEP}}$  for low  $\kappa_\ell^{\text{TDEP}}$  compounds, and vice versa for high  $\kappa_\ell^{\text{TDEP}}$  compounds. This is also seen with the logarithmic view of Fig. 6 (a). Even if the numerical precision of the active sampling model for the low  $\kappa_\ell^{\text{TDEP}}$  compounds remains quite modest, which can be linked to a limited sampling in this region of feature space, the method clearly identifies the compounds with the lowest  $\kappa_\ell^{\text{TDEP}}$ . Appendix A Table A.1 provides a complete comparison between  $\kappa_\ell^{\text{TDEP}}$  and  $\kappa_\ell^{\text{AS}}$ .

Table 1 summarizes various ML performance metrics. As the ranking of compounds is the primary

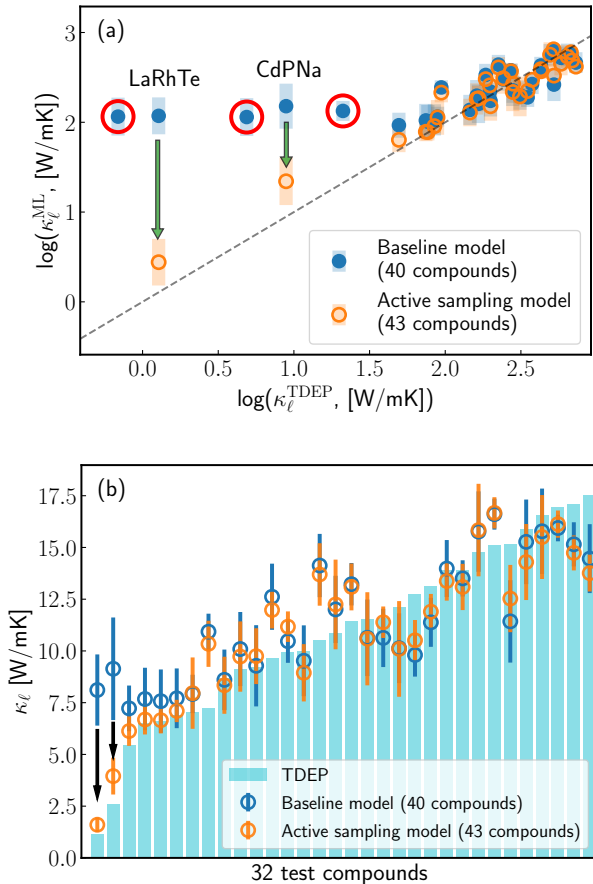


Fig. 6: a) Parity plot for predictions made on the test set. The x-axis shows  $\log(\kappa_{\ell}^{\text{TDEP}})$  at 500 K, while the y-axis shows the predictions. Blue (orange) circles indicate the predictions made by the baseline (active sampling) model. Predictions for BaBiK, LaPtSb and LiZnSb are not shown for the active sampling model. b) Corresponding comparison for  $\kappa_{\ell}^{\text{TDEP}}$ . The turquoise bars indicate  $\kappa_{\ell}^{\text{TDEP}}$  at 500 K.

target in this study, we first discuss the Spearman correlation. The baseline model predictions,  $\log(\kappa_{\ell}^{\text{BL}})$ , has a Spearman correlation of 0.77 with  $\log(\kappa_{\ell}^{\text{TDEP}})$ , which is larger than the correlation of Carrete et al. [18] of 0.74. Their model is based on few training samples, but with more complex features. However, even though the Spearman correlation met-

ric is fair and the low  $\kappa_{\ell}^{\text{TDEP}}$  compounds do tend to be in the lower end of the spectrum of  $\log(\kappa_{\ell}^{\text{BL}})$ , the model fails to differentiate between the truly low lattice thermal conductivity compounds and the rest. The active sampling model has a superior ability to identify such compounds, but also has superior predictivity for most other compounds, as reflected in the improvement of the other performance metrics.

While the performance gain when using more complex features and larger training sets has been demonstrated in earlier studies [20–23, 70–73], this work clearly shows that rather modest training set sizes and low feature complexity can still give reliable predictions with the use of active sample selection. Finally, we note that the use of a semi-random selection, rather than one that is truly random do accentuate the performance gains of the active sampling model. Nonetheless, we find that only including some of the low lattice thermal conductivity compounds in the model significantly reduces performance compared to including all three. Performance with a truly random model could also be very sensitive to exactly which training samples are selected. In any case, a key advantage of PCA is that when used in the process to include additional half-Heusler compounds, we have a procedure to identify whether the properties of a given compound can be predicted reliably.

#### 4. Summary and conclusion

This study has explored strategies for using machine learning for finding low lattice thermal conductivity compounds using a limited number of training samples. Moreover, rather simple features was used, which can found directly in material databases or computed straightforwardly. The exploration was made possible by computing lattice thermal conductivity with the temperature dependent effective potential method for 122 half-Heusler compounds. We first demonstrated how a model based on a semi-random pool of materials (i.e. assumed "bad luck" in the training set) was unable to separate the truly low lattice thermal conductivity compounds in the test set from the rest. To improve the model, we used active sample selection based on principal component analysis. This approach suggested three com-

pounds to be included in the training process. The subsequent inclusions resulted in a substantial improvement of the model performance, in particular the ability to identify the remaining low lattice thermal conductivity compounds in the test set. Our study demonstrates how active sampling can improve the ability to accurately predict properties of compounds dissimilar from the typical ones in a material class. More narrowly, we expect the procedure outlined here to be adopted to study broader classes of materials to systematically identify new low lattice thermal conductivity compounds.

## 5. Data Availability

The lattice thermal conductivities for the HH compounds calculated with the TDEP method are available in Appendix A Table A.1.

## Acknowledgements

The computations in this work were done on the high performance cluster Saga managed by UNINETT Sigma2. This work is part of the Al-therm project (Project No. 314778) supported by the Research Council of Norway.

## Appendix A. Lattice thermal conductivity

Table A.1 shows  $\kappa_{\ell}^{\text{TDEP}}$  for the HH compounds. Predictions made with the active sampling model are in the parenthesis.

## References

- [1] G. J. Snyder, E. S. Toberer, Complex thermoelectric materials, *Nat. Mater.* 7 (2) (2008) 105–114. doi:10.1038/nmat2090.
- [2] D. Champier, Thermoelectric generators: A review of applications, *Energy Convers. Manag.* 140 (2017) 167–181. doi:10.1016/j.enconman.2017.02.070.
- [3] J. J. G. Moreno, A review of recent progress in thermoelectric materials through computational methods, *Mater. Renew. Sustain. Energy* (2020) 22doi:10.1007/s40243-020-00175-5.
- [4] J. Wei, L. Yang, Z. Ma, P. Song, M. Zhang, J. Ma, F. Yang, X. Wang, Review of current high-ZT thermoelectric materials, *J Mater Sci* 55 (27) (2020) 12642–12704. doi:10.1007/s10853-020-04949-0.
- [5] J. Recatala-Gomez, A. Suwardi, I. Nandhakumar, A. Abutaha, K. Hippalgaonkar, Toward accelerated thermoelectric materials and process discovery, *ACS Appl. Energy Mater.* 3 (3) (2020) 2240–2257. doi:10.1021/acsaem.9b02222.
- [6] P. P. Paskov, M. Slomski, J. H. Leach, J. F. Muth, T. Paskova, Effect of Si doping on the thermal conductivity of bulk GaN at elevated temperatures – theory and experiment, *AIP Advances* 7 (9) (2017) 095302. doi:10.1063/1.4989626.
- [7] S. Y. Kim, H.-S. Kim, K. H. Lee, H.-j. Cho, S.-s. Choo, S.-w. Hong, Y. Oh, Y. Yang, K. Lee, J.-H. Lim, S.-M. Choi, H. J. Park, W. H. Shin, S.-i. Kim, Influence of Pd doping on electrical and thermal properties of n-type  $\text{Cu}_{0.008}\text{Bi}_2\text{Te}_{2.7}\text{Se}_{0.3}$  alloys, *Materials* 12 (24) (2019) 4080. doi:10.3390/ma12244080.
- [8] K. Berland, N. Shulumba, O. Hellman, C. Persson, O. M. Løvvik, Thermoelectric transport trends in group 4 half-Heusler alloys, *J. Appl. Phys.* 126 (14) (2019) 145102. arXiv:https://doi.org/10.1063/1.5117288.
- [9] R. Li, X. Li, L. Xi, J. Yang, D. J. Singh, W. Zhang, High-throughput screening for advanced thermoelectric materials: diamond-like  $\text{ABX}_2$  compounds, *ACS Appl. Mater. Interfaces* 11 (28) (2019) 24859–24866. doi:10.1021/acsaami.9b01196.
- [10] K. Choudhary, K. F. Garrity, F. Tavazza, Data-driven discovery of 3D and 2D thermoelectric materials, *J. Condens. Matter Phys.* 32 (47)

- (2020) 475501. doi:10.1088/1361-648X/aba06b.
- [11] J. Liu, S. Han, G. Cao, Z. Zhou, C. Sheng, H. Liu, A high-throughput descriptor for prediction of lattice thermal conductivity of half-Heusler compounds, *J. Phys. D: Appl. Phys.* 53 (31) (2020) 315301. doi:10.1088/1361-6463/ab898e.
- [12] J. He, M. Amsler, Y. Xia, S. S. Naghavi, V. I. Hegde, S. Hao, S. Goedecker, V. Ozoliņš, C. Wolverton, Ultralow thermal conductivity in full Heusler semiconductors, *Phys. Rev. Lett.* 117 (4) (2016) 046602. doi:10.1103/PhysRevLett.117.046602.
- [13] P. R. Raghuvanshi, S. Mondal, A. Bhattacharya, A high throughput search for efficient thermoelectric half-Heusler compounds, *J. Mater. Chem. A* 8 (47) (2020) 25187–25197. doi:10.1039/D0TA06810A.
- [14] T.-T. Jia, Z. Feng, S. Guo, X. Zhang, Y. Zhang, Screening promising thermoelectric materials in binary chalcogenides through high-throughput computations, *ACS Appl. Mater. Interfaces* 12 (2020) 11852–11864. doi:10.1021/acsami.9b23297.
- [15] A. Togo, L. Chaput, I. Tanaka, Distributions of phonon lifetimes in Brillouin zones, *Phys. Rev. B* 91 (9) (2015) 094306. doi:10.1103/PhysRevB.91.094306.
- [16] O. Hellman, I. A. Abrikosov, Temperature-dependent effective third-order interatomic force constants from first principles, *Phys. Rev. B* 88 (14) (2013) 144301. doi:10.1103/PhysRevB.88.144301.
- [17] F. Zhou, W. Nielson, Y. Xia, V. Ozoliņš, Lattice anharmonicity and thermal conductivity from compressive sensing of first-principles calculations, *Phys. Rev. Lett.* 113 (18) (2014) 185501. doi:10.1103/PhysRevLett.113.185501.
- [18] J. Carrete, W. Li, N. Mingo, S. Wang, S. Curtarolo, Finding unprecedentedly low-thermal-conductivity half-Heusler semiconductors via high-throughput materials modeling, *Phys. Rev. X* 4 (1) (2014) 011019. doi:10.1103/PhysRevX.4.011019.
- [19] S. Ju, R. Yoshida, C. Liu, K. Hongo, T. Tadano, Exploring diamond-like lattice thermal conductivity crystals via feature-based transfer learning (2019) 27doi:10.1103/PhysRevMaterials.5.053801.
- [20] L. Chen, H. Tran, R. Batra, C. Kim, R. Ramprasad, Machine learning models for the lattice thermal conductivity prediction of inorganic materials, *Comput. Mater. Sci.* 170 (2019) 109155. doi:10.1016/j.commatsci.2019.109155.
- [21] X. Wang, S. Zeng, Z. Wang, J. Ni, Identification of crystalline materials with ultra-low thermal conductivity based on machine learning study, *J. Phys. Chem. C* 124 (16) (2020) 8488–8495. doi:10.1021/acs.jpcc.9b11610.
- [22] C. Loftis, K. Yuan, Y. Zhao, M. Hu, J. Hu, Lattice thermal conductivity prediction using symbolic regression and machine learning, *J. Phys. Chem. A* 125 (1) (2021) 435–450. doi:10.1021/acs.jpca.0c08103.
- [23] T. Zhu, R. He, S. Gong, T. Xie, P. Gorai, K. Nielsch, J. C. Grossman, Charting lattice thermal conductivity for inorganic crystals and discovering rare earth chalcogenides for thermoelectrics, *Energy Environ. Sci.* 14 (2021) 3559–3566. doi:10.1039/D1EE00442E.
- [24] D. Visaria, A. Jain, Machine-learning-assisted space-transformation accelerates discovery of high thermal conductivity alloys, *Appl. Phys. Lett.* 117 (20) (2020) 202107. doi:10.1063/5.0028241.
- [25] C. M. Collins, L. M. Daniels, Q. Gibson, M. W. Gaultois, M. Moran, R. Feetham, M. J. Pitcher, M. S. Dyer, C. Delacotte, M. Zanella, C. A. Murray, G. Glodan, O. Pérez, D. Pelloquin, T. D.

- Manning, J. Alaria, G. R. Darling, J. B. Claridge, M. J. Rosseinsky, Discovery of a low thermal conductivity oxide guided by probe structure prediction and machine learning, *Angew. Chem. Int. Ed* (2021). doi:<https://doi.org/10.1002/anie.202102073>.
- [26] M. W. Gaultois, A. O. Oliynyk, A. Mar, T. D. Sparks, G. J. Mulholland, B. Meredig, A recommendation engine for suggesting unexpected thermoelectric chemistries, *APL Mater.* 4 (5) (2016) 053213, arXiv: 1502.07635. doi:10.1063/1.4952607.
- [27] F. Casper, T. Graf, S. Chadov, B. Balke, C. Felser, Half-Heusler compounds: novel materials for energy and spintronic applications, *Semicond. Sci. Technol.* 27 (6) (2012) 063001. doi:10.1088/0268-1242/27/6/063001.
- [28] J.-W. G. Bos, R. A. Downie, Half-Heusler thermoelectrics: a complex class of materials, *J. Condens. Matter Phys.* 26 (43) (2014) 433201. doi:10.1088/0953-8984/26/43/433201.
- [29] T. Zhu, C. Fu, H. Xie, Y. Liu, X. Zhao, High efficiency half-Heusler thermoelectric materials for energy harvesting, *Adv. Energy Mater.* 5 (19) (2015) 1500588. doi:10.1002/aenm.201500588.
- [30] B. Yuan, B. Wang, L. Huang, X. Lei, L. Zhao, C. Wang, Q. Zhang, Effects of Sb substitution by Sn on the thermoelectric properties of ZrCoSb, *J. Electron. Mater.* 46 (5) (2017) 3076-3082. doi:10.1007/s11664-016-5168-z.
- [31] A. Hori, S. Minami, M. Saito, F. Ishii, First-principles calculation of lattice thermal conductivity and thermoelectric figure of merit in ferromagnetic half-Heusler alloy CoMnSb, *Appl. Phys. Lett.* 116 (24) (2020) 242408. doi:10.1063/1.5143038.
- [32] N. S. Chauhan, P. R. Raghuvanshi, K. Tyagi, K. K. Johari, L. Tyagi, B. Gahtori, S. Bathula, A. Bhattacharya, S. D. Mahanti, V. N. Singh, Y. V. Kolen'ko, A. Dhar, Defect engineering for enhancement of thermoelectric performance of (Zr, Hf)NiSn-Based n-type half-Heusler alloys, *J. Phys. Chem. C* 124 (16) (2020) 8584-8593. doi:10.1021/acs.jpcc.0c00681.
- [33] H. Zhu, J. Mao, Y. Li, J. Sun, Y. Wang, Q. Zhu, G. Li, Q. Song, J. Zhou, Y. Fu, R. He, T. Tong, Z. Liu, W. Ren, L. You, Z. Wang, J. Luo, A. Sotnikov, J. Bao, K. Nielsch, G. Chen, D. J. Singh, Z. Ren, Discovery of TaFeSb-based half-Heuslers with high thermoelectric performance, *Nat. Commun.* 10 (1) (2019) 270. doi:10.1038/s41467-018-08223-5.
- [34] H.-L. Sun, C.-L. Yang, M.-S. Wang, X.-G. Ma, Remarkably high thermoelectric efficiencies of the half-Heusler compounds BXGa (X = Be, Mg, and Ca), *ACS Appl. Mater. Interfaces* 12 (5) (2020) 5838-5846. doi:10.1021/acsami.9b19198.
- [35] D. Zhao, M. Zuo, Z. Wang, X. Teng, H. Geng, Synthesis and thermoelectric properties of tantalum-doped ZrNiSn half-Heusler alloys, *Funct. Mater. Lett.* 07 (03) (2014) 1450032. doi:10.1142/S1793604714500325.
- [36] J. Zhou, H. Zhu, T.-H. Liu, Q. Song, R. He, J. Mao, Z. Liu, W. Ren, B. Liao, D. J. Singh, Z. Ren, G. Chen, Large thermoelectric power factor from crystal symmetry-protected non-bonding orbital in half-Heuslers, *Nat. Commun.* 9 (2018). doi:10.1038/s41467-018-03866-w.
- [37] Z. Feng, Y. Fu, Y. Zhang, D. J. Singh, Characterization of rattling in relation to thermal conductivity: ordered half-Heusler semiconductors, *Phys. Rev. B* 101 (6) (2020) 064301, arXiv: 2001.08029. doi:10.1103/PhysRevB.101.064301.
- [38] Q. Y. Xue, H. J. Liu, D. D. Fan, L. Cheng, B. Y. Zhao, J. Shi, LaPtSb: a half-Heusler compound with high thermoelectric performance, *Phys. Chem. Chem. Phys.* 18 (27) (2016) 17912-17916. doi:10.1039/C6CP03211G.
- [39] S. H. Han, Z. Z. Zhou, C. Y. Sheng, J. H. Liu, L. Wang, H. M. Yuan, H. J. Liu,

- High thermoelectric performance of half-Heusler compound BiBaK with intrinsically low lattice thermal conductivity, *J. Condens. Matter Phys.* 32 (42) (2020) 425704. doi:10.1088/1361-648X/aba2e7.
- [40] G. Samsonidze, B. Kozinsky, Accelerated screening of thermoelectric materials by first-principles computations of electron-phonon scattering, *Adv. Energy Mater.* 8 (20) (2018) 1800246. doi:10.1002/aenm.201800246.
- [41] S. Zhang, B. Xu, Y. Lin, C. Nan, W. Liu, First-principles study of the layered thermoelectric material TiNBr, *RSC Adv.* 9 (23) (2019) 12886–12894. doi:10.1039/C9RA00247B.
- [42] D. Sarkar, T. Ghosh, S. Roychowdhury, R. Arora, S. Sajan, G. Sheet, U. V. Waghmare, K. Biswas, Ferroelectric instability induced ultralow thermal conductivity and high thermoelectric performance in rhombohedral *p*-Type GeSe crystal, *J. Am. Chem. Soc.* 142 (28) (2020) 12237–12244. doi:10.1021/jacs.0c03696.
- [43] L.-D. Zhao, S.-H. Lo, Y. Zhang, H. Sun, G. Tan, C. Uher, C. Wolverton, V. P. Dravid, M. G. Kanatzidis, Ultralow thermal conductivity and high thermoelectric figure of merit in SnSe crystals, *Nature* 508 (7496) (2014) 373–377. doi:10.1038/nature13184.
- [44] G. Kresse, J. Hafner, *Ab initio* molecular dynamics for liquid metals, *Phys. Rev. B* 47 (1) (1993) 558–561. doi:10.1103/PhysRevB.47.558.
- [45] G. Kresse, J. Furthmüller, Efficiency of ab-initio total energy calculations for metals and semiconductors using a plane-wave basis set, *Comput. Mater. Sci.* 6 (1) (1996) 15–50. doi:10.1016/0927-0256(96)00008-0.
- [46] G. Kresse, J. Furthmüller, Efficient iterative schemes for *ab initio* total-energy calculations using a plane-wave basis set, *Phys. Rev. B* 54 (16) (1996) 11169–11186. doi:10.1103/PhysRevB.54.11169.
- [47] J. P. Perdew, A. Ruzsinszky, G. I. Csonka, O. A. Vydrov, G. E. Scuseria, L. A. Constantin, X. Zhou, K. Burke, Restoring the density-gradient expansion for exchange in solids and surfaces, *Phys. Rev. Lett.* 100 (13) (2008) 136406. doi:10.1103/PhysRevLett.100.136406.
- [48] G. I. Csonka, J. P. Perdew, A. Ruzsinszky, P. H. T. Philipsen, S. Lebègue, J. Paier, O. A. Vydrov, J. G. Ángyán, Assessing the performance of recent density functionals for bulk solids, *Phys. Rev. B* 79 (15) (2009) 155107. doi:10.1103/PhysRevB.79.155107.
- [49] O. Hellman, I. A. Abrikosov, S. I. Simak, Lattice dynamics of anharmonic solids from first principles, *Phys. Rev. B* 84 (18) (2011) 180301. doi:10.1103/PhysRevB.84.180301.
- [50] S.-i. Tamura, Isotope scattering of dispersive phonons in Ge, *Phys. Rev. B* 27 (2) (1983) 858–866. doi:10.1103/PhysRevB.27.858.
- [51] S.-i. Tamura, Isotope scattering of large-wave-vector phonons in GaAs and InSb: Deformation-dipole and overlap-shell models, *Phys. Rev. B* 30 (2) (1984) 849–854. doi:10.1103/PhysRevB.30.849.
- [52] N. Shulumba, O. Hellman, A. J. Minnich, Intrinsic localized mode and low thermal conductivity of PbSe, *Phys. Rev. B* 95 (2017) 014302. doi:10.1103/PhysRevB.95.014302.
- [53] O. Anderson, A simplified method for calculating the debye temperature from elastic constants, *J Phys Chem Solids* 24 (7) (1963) 909–917. doi:10.1016/0022-3697(63)90067-2.
- [54] L. Breiman, Random forests, *Mach. Learn.* 45 (1) (2001) 5–32. doi:10.1023/A:1010933404324.
- [55] S. Raschka, V. Mirjalili, Python machine learning: machine learning and deep learning with Python, Scikit-Learn, and TensorFlow, 2nd Edition, 2nd Edition, Packt Publishing, 2017.

- [56] H. K. Jabbar, R. Z. Khan, Methods to avoid over-fitting and under-fitting in supervised machine learning (comparative study), in: *Computer Science, Communication and Instrumentation Devices*, Research Publishing Services, 2014, pp. 163–172. doi:10.3850/978-981-09-5247-1\\_017.
- [57] S. Raschka, MLxtend: Providing machine learning and data science utilities and extensions to Python’s scientific computing stack, *JOSS* 3 (24) (2018) 638. doi:10.21105/joss.00638.
- [58] F. Pedregosa, G. Varoquaux, A. Gramfort, V. Michel, B. Thirion, O. Grisel, M. Blondel, P. Prettenhofer, R. Weiss, V. Dubourg, J. Vanderplas, A. Passos, D. Cournapeau, Scikit-learn: machine learning in Python, *J. Mach. Learn. Res.* 12 (2011) 2825.
- [59] O. Tomic, T. Graff, K. Liland, T. Næs, Hoggorm: a python library for explorative multivariate statistics, *JOSS* 4 (39) (2019) 980. doi:10.21105/joss.00980.
- [60] J. Meija, T. Coplen, M. Berglund, W. Brand, P. De Bièvre, M. Gröning, N. Holden, J. Irrgeher, R. Loss, T. Walczyk, T. Prohaska, Atomic weights of the elements 2013 (iupac technical report), *Pure Appl. Chem.* 88 (2016) 265–291. doi:10.1515/pac-2015-0305.
- [61] L. C. Allen, Electronegativity is the average one-electron energy of the valence-shell electrons in ground-state free atoms, *J. Am. Chem. Soc.* 111 (1989) 9003–9014. doi:10.1021/JA00207A003.
- [62] B. Cordero, V. Gómez, A. Platero-Prats, M. Revés, J. Echeverría, E. Cremades, F. Barragán, S. Alvarez, Covalent radii revisited, *Dalton trans.* 21 (2008) 2832–8. doi:10.1039/b801115j.
- [63] G. A. Slack, Nonmetallic crystals with high thermal conductivity, *J Phys Chem Solids* 34 (2) (1973) 15. doi:10.1016/0022-3697(73)90092-9.
- [64] T. Jia, G. Chen, Y. Zhang, Lattice thermal conductivity evaluated using elastic properties, *Phys. Rev. B* 95 (15) (2017) 155206. doi:10.1103/PhysRevB.95.155206.
- [65] S. Ju, J. Shiomi, Materials informatics for heat transfer: recent progresses and perspectives, *Nanoscale Microscale Thermophys. Eng.* 23 (2) (2019) 157–172. doi:10.1080/15567265.2019.1576816.
- [66] A. Jain, S. P. Ong, G. Hautier, W. Chen, W. D. Richards, S. Dacek, S. Cholia, D. Gunter, D. Skinner, G. Ceder, K. A. Persson, Commentary: The Materials Project: A materials genome approach to accelerating materials innovation, *APL Mater.* 1 (1) (2013) 011002. doi:10.1063/1.4812323.
- [67] R. Gautier, X. Zhang, L. Hu, L. Yu, Y. Lin, T. O. L. Sunde, D. Chon, K. R. Poeppelmeier, A. Zunger, Prediction and accelerated laboratory discovery of previously unknown 18-electron ABX compounds, *Nature Chem* 7 (4) (2015) 308–316. doi:10.1038/nchem.2207.
- [68] M. W. Gaultois, T. D. Sparks, How much improvement in thermoelectric performance can come from reducing thermal conductivity?, *Appl. Phys. Lett.* 104 (11) (2014) 113906. doi:10.1063/1.4869232.
- [69] J. An, A. Subedi, D. Singh, Ab initio phonon dispersions for PbTe, *Solid State Commun.* 148 (9–10) (2008) 417–419. doi:10.1016/j.ssc.2008.09.027.
- [70] H. Miyazaki, T. Tamura, M. Mikami, K. Watanabe, N. Ide, O. M. Ozkendir, N. Toichi, Machine learning based prediction of lattice thermal conductivity for half-Heusler compounds using atomic information, *Sci. Rep.* (2021) 8doi:https://doi.org/10.1038/s41598-021-92030-4.
- [71] R. Juneja, G. Yumnam, S. Satsangi, A. K. Singh, Coupling the high-throughput property map to machine learning for predicting lattice thermal

conductivity, *Chem. Mater.* 31 (14) (2019) 5145–5151. doi:10.1021/acs.chemmater.9b01046.

[72] R. Juneja, A. K. Singh, Guided patchwork kriging to develop highly transferable thermal conductivity prediction models, *J. Phys. Mater.* 3 (2) (2020) 024006. doi:10.1088/2515-7639/ab78f2.

[73] A. Tewari, S. Dixit, N. Sahni, S. P. Bordas, Machine learning approaches to identify and design low thermal conductivity oxides for thermoelectric applications, *DCE* 1 (2020) e8. doi:10.1017/dce.2020.7.

Table A.1: Calculated  $\kappa_{\ell}^{\text{DEP}}$  at 500 K for the HHs. The 32 compounds in the final test set are highlighted with bold text, and predictions made with the active sampling model are in parenthesis.

$\kappa_{\ell}$ [W/mK]	$\kappa_{\ell}$ [W/mK]	$\kappa_{\ell}$ [W/mK]	$\kappa_{\ell}$ [W/mK]
LaPtSb 0.85	ZrPtGe 8.27	<b>ZrCoBi</b> 11.54 (10.59)	TaCoGe 15.47
<b>LaRhTe</b> 1.11 (1.60)	TiPdSn 8.42	<b>NbIrSn</b> 11.57 (11.39)	VRuAs 15.52
BaBiK 1.99	<b>NbRuBi</b> 8.70 (8.34)	HfCoAs 11.64	TiPdGe 15.78
<b>CdPNa</b> 2.58 (3.95)	TiPtSn 8.88	TiRhSb 11.72	<b>GaNiNb</b> 15.88 (14.30)
LiZnSb 3.76	HfIrAs 9.04	HfRhAs 11.76	NbOsAs 15.95
TaIrPb 5.20	<b>ZrNiPb</b> 9.10 (9.73)	TaIrSn 11.84	SiCoTa 16.28
TiPtPb 5.43	VOsSb 9.12	NbOsSb 11.86	<b>VRhGe</b> 16.57 (15.50)
<b>BiPdSc</b> 5.44 (6.13)	AlSiLi 9.18	ZrRhSb 11.89	VCoGe 16.58
BiNiY 5.46	<b>ZrPtSn</b> 9.20 (9.75)	<b>HfCoBi</b> 12.11 (10.10)	TaRuAs 16.60
HfPtPb 5.48	HfPdSn 9.32	NbCoSn 12.23	GaPtTa 16.75
HfPdPb 5.86	VRuSb 9.32	TaFeBi 12.40	VOsAs 16.82
TaOsBi 5.90	ZrPdSn 9.37	HfCoSb 12.48	TaRhGe 16.85
TiPdPb 5.94	AsNiSc 9.46	ZrNiGe 12.48	<b>VIrGe</b> 16.95 (16.13)
TaRhPb 5.95	<b>TaCoPb</b> 9.66 (11.98)	NbRuSb 12.52	GeFeW 17.07
NbIrPb 6.07	<b>NbRhSn</b> 9.92 (11.17)	<b>TiIrSb</b> 12.73 (10.51)	<b>TaFeSb</b> 17.10 (14.74)
<b>ZrPtPb</b> 6.50 (6.69)	NbCoPb 9.95	<b>TaRuSb</b> 13.12 (11.90)	AlAuHf 17.11
HfIrBi 6.58	<b>HfNiPb</b> 9.96 (8.94)	TaCoSn 13.38	NbIrGe 17.21
<b>ZrPdPb</b> 6.59 (6.65)	HfPtSn 9.98	VFeSb 13.40	<b>TiRhAs</b> 17.52 (13.76)
TiIrBi 6.68	HfPdGe 10.28	HfIrSb 13.65	TaOsAs 18.09
<b>ZrIrBi</b> 6.88 (7.10)	<b>TiNiSn</b> 10.50 (13.69)	TeFeTi 13.82	TiCoBi 19.10
BiNiSc 6.97	<b>ZrNiSn</b> 10.84 (12.25)	<b>TiCoSb</b> 13.90 (13.38)	NbCoGe 19.37
HfRhBi 7.00	ZrIrSb 10.97	TiNiPb 13.91	TaIrGe 19.57
VIrSn 7.01	ZrPdGe 10.98	<b>ZrCoAs</b> 13.91 (13.09)	TiCoAs 19.92
<b>TaRuBi</b> 7.02 (7.96)	HfPtGe 11.08	TiIrAs 14.12	NbRuAs 20.21
VRhSn 7.11	TeRuZr 11.11	ZrCoSb 14.29	NbCoSi 20.31
<b>ZrIrAs</b> 7.20 (10.34)	HfNiSn 11.29	TiPtGe 14.34	NbRhGe 20.63
NbRhPb 7.21	VCoSn 11.30	ZrRhAs 14.54	NbFeAs 22.20
NbOsBi 7.26	TaRhSn 11.37	<b>TiNiGe</b> 14.78 (15.84)	VFeAs 22.60
ZrRhBi 7.33	NbFeBi 11.40	NbFeSb 15.00	LiBSi 23.45
AlGeLi 7.68	<b>HfNiGe</b> 11.41 (13.09)	<b>TaFeAs</b> 15.12 (16.67)	
TiRhBi 7.85	HfRhSb 11.49	<b>TaOsSb</b> 15.16 (12.53)	